Journal of
Materials Chemistry A

ROYAL SOCIETY
OF CHEMISTRY

COMMUNICATION

View Article Online
View Journal

Check for updates

Cite this: DOI: 10.1039/d6ta01055e

Received 3rd February 2026
Accepted 22nd April 2026

DOI: 10.1039/d6ta01055e

rsc.li/materials-a

In situ growth of mixed-valence 2D α-MnO_x nanosheets within interlayer spaces of multilayer Ti_3C_2 MXene as an efficient air cathode for rechargeable Li–O_2 batteries

Aqrab ul Ahmad, †[a] William G. Morais, †[a] Tauqeer Ahmad,[ab] Ihsan Çaha, [a]
Isilda Amorim, [a] Siva Sankar Nemala [a] and Francis Leonard Deepak *[a]

Rechargeable Li–O_2 batteries are promising options for energy storage systems due to their simple fabrication, non-toxicity, and low cost. Herein, we present a new cathode design for Li–O_2 batteries, featuring non-stoichiometric, mixed-valence 2D α-MnO_x nanosheets ($Mn^{4+}/Mn^{3+}/Mn^{2+}$) confined within multilayered MXene (M–Ti_3C_2). Electrochemical results show that the 2D α-MnO_x@M–Ti_3C_2 electrode achieved a specific capacity of up to 14 377 mAh g^{-1} at 100 mA g^{-1} and remained stable over 54 cycles at 500 mA g^{-1} (with a 500 mA g^{-1} cutoff). This approach enables the design of manganese oxide-based cathodes within a conductive MXene scaffold for high-performance Li–O_2 batteries.

Over the past decades, lithium–air (Li–O_2) batteries (LABs) have been considered among the most promising alternatives to lithium-ion batteries (LIBs) for energy storage systems, with the aim of supporting the transition toward a fully decarbonized global energy matrix.[1] This interest is largely driven by their exceptionally high theoretical energy density of 3500 W h kg^{-1}, based on the formation of Li_2O_2, nearly 10 times that of the 250 W h kg^{-1} achievable with LIBs.[2,3] However, significant hysteresis between discharge and charge potentials is commonly observed in LABs operation, primarily due to weak interactions between the active cathode material and the discharge product, Li_2O_2.[4,5] This results in low round-trip efficiency, as the lithium ions are only partially recovered after a complete charge–discharge cycle. To achieve commercially viable LABs, key challenges related to the air cathode must be addressed. These include, but are not limited to, high electronic conductivity, vigorous catalytic activity for Oxygen Reduction and Evolution Reaction (ORR/OER), electrochemical stability, a high surface area, and cost-effectiveness.[2]

Manganese-based oxides (MnO_x) are highly promising electrocatalysts for LABs electrochemistry due to several factors. Their multiple valence states enable a variety of crystal structures, contributing to excellent catalytic activity for both the ORR and OER.[6,7] Additionally, MnO_x is abundant, cost-effective, environmentally friendly, and has low-toxicity.[8] The effect of MnO_2 on the performance of LABs cathodes was reported by Read,[9] followed by Bruce and colleagues, who demonstrated that the presence of manganese oxides facilitates the decomposition of Li_2O_2 into Li^+ and O_2 during the charging process.[10] Since then, various MnO_2 crystalline structures, including α-MnO_2, β-MnO_2, γ-MnO_2, ε-MnO_2, δ-MnO_2, and λ-MnO_2, in addition to MnO, Mn_2O_3,[11] Mn_3O_4, and γ-MnOOH, have been explored as LABs electrode catalysts, exhibiting enhanced electrochemical activity.[12]

Various strategies have been employed to synergistically combine MnO_x electrocatalytic properties with MXene's structural stability to enhance ORR/OER activity, and durability for energy storage applications.[13] Regarding ORR/OER and energy storage, Xue *et al.*[14] successfully grew Mn_3O_4 nanoparticles on a layered Ti_3C_2 MXene by etching an Al layer with HF at a mild temperature, thereby enhancing conductivity and reaction kinetics in a zinc–air system. Similarly, Sun *et al.*[15] explored the ORR activity of a MnO_x@$Ti_3C_2T_x$ composite with oxygen vacancies created by lithium reduction. When used as an electrode in a Zn–air battery (ZAB), the composite delivered cycling performance superior to that of Pt/C air cathodes while maintaining good structural stability. Although the use of MnO_x@-MXene composites as air cathodes for ZAB has been recently demonstrated, there are no similar reports for LAB despite the promising electrocatalytic properties of these materials. The practical use of MnO_2-based cathodes however is hindered by their low electrical conductivity and poor cycling stability and hence there is room for improving these characteristics.[16]

Herein, we present a low-temperature, *in situ* method for synthesizing α-MnO_x within Ti_3C_2 MXene layers by combining $MnCl_2$ and potassium borate during dimethyl sulfoxide (DMSO)-assisted delamination at 40 °C. In this method, borate

---

[a] *International Iberian Nanotechnology Laboratory (INL), Avenida Mestre Jose Veiga, Braga 4715-330, Portugal. E-mail: leonard.francis@inl.int*

[b] *Department of Chemical and Biological Engineering, University of Porto, Faculty of Engineering, Rua dr. Roberto Frias, 4200-465 Porto, Portugal*

† Authors contributed equally.

anions, DMSO, and M–Ti_3C_2 surface terminations facilitate a cooperative, low-temperature oxidation of Mn^{2+} to Mn^{3+}/Mn^{4+}, thereby promoting the formation of confined mixed-valence α-MnO_x nanosheets within the MXene interlayers. The resulting hybrid nanosheet electrodes exhibit outstanding electrocatalytic performance for Li–O_2 batteries, surpassing other MnO_2-based hybrids, including those with α-MnO_2, as detailed in Table S1 of the SI. The impressive performance of these multilayer 2D α-MnO_x@Ti_3C_2 hybrid nanosheets highlights the potential of our heterolayer hybridization approach, making them highly effective as Li–O_2 battery electrodes.

The Multilayered M–Ti_3C_2 MXene suspension was synthesized *via* the previously reported molten-salt methods[17] For the growth of 2D α-MnO_x nanosheets within the etched spaces of M–Ti_3C_2, a low-temperature wet chemical route was adopted (see SI for the detailed procedure). The *in situ* formation of multivalent 2D α-MnO_x nanosheets within $Ti_3C_2T_x$ layers arises from ion intercalation, oxidative transformation, and 2D crystallization driven by confinement. When $MnCl_2$ is mixed with $Ti_3C_2T_x$ in DMSO containing potassium borate, Mn^{2+} ions readily intercalate into the negatively charged MXene layers *via* electrostatic attraction and solvent swelling. At 40 °C, the borate buffer ($B(OH)_4^-/B(OH)_3$) creates mildly alkaline regions where dissolved oxygen oxidizes Mn^{2+} to Mn^{4+} *via* the reaction: $2\ Mn^{2+} + O_2 + 4\ OH^- \rightarrow 2\ MnO_2 + 2\ H_2O$. Simultaneously, surface groups on MXene (–O, –OH, –F) donate electrons that partially reduce Mn, forming MnO_x nuclei, resulting in a mixture of $Mn^{4+}/Mn^{3+}/Mn^{2+}$, as shown by XPS (Fig. 3 and S2). Since oxidation and redox equilibrium occur within angstrom-scale interlayers, the limited space prevents out-of-plane growth, causing Mn–O octahedra to assemble laterally into 2D α-MnO_x nanosheets.

The crystallographic structure of the synthesized 2D α-MnO_x@M–Ti_3C_2 sample was examined using XRD and Raman spectroscopy. Fig. 1(a) shows the XRD pattern of the 2D α-MnO_x@Ti_3C_2 hybrid nanosheets, which features a low-angle shift of the (002) reflection plane of Ti_3C_2 MXene, along with distinct diffraction peaks corresponding to α-MnO_2. This confirms the successful formation of MnO_x nanosheets within the expanded multilayered MXene interlayers. The clear α-MnO_x reflections, such as (200), (310), and (400), suggest that α-MnO_2 was grown and closely integrated with the layered M–Ti_3C_2 framework. Raman analysis further elucidates the interfacial interactions and the evolution of surface chemistry during electrochemical cycling. The spectrum is divided into four regions: the flake region (100–250 cm^{-1}), the T_x region (220–500 cm^{-1}), the α-MnO_x region (510–650 cm^{-1}), and the carbon region (650–1000 cm^{-1}), as shown in Fig. 1(c). The flake region indicates the vibrations of Ti, C, and surface groups. In contrast, the T_x region involves surface termination modes such as –O and –OH.[18] In the case of the pristine sample, the 2D α-MnO_x@M–Ti_3C_2 electrode shows broad features that come from

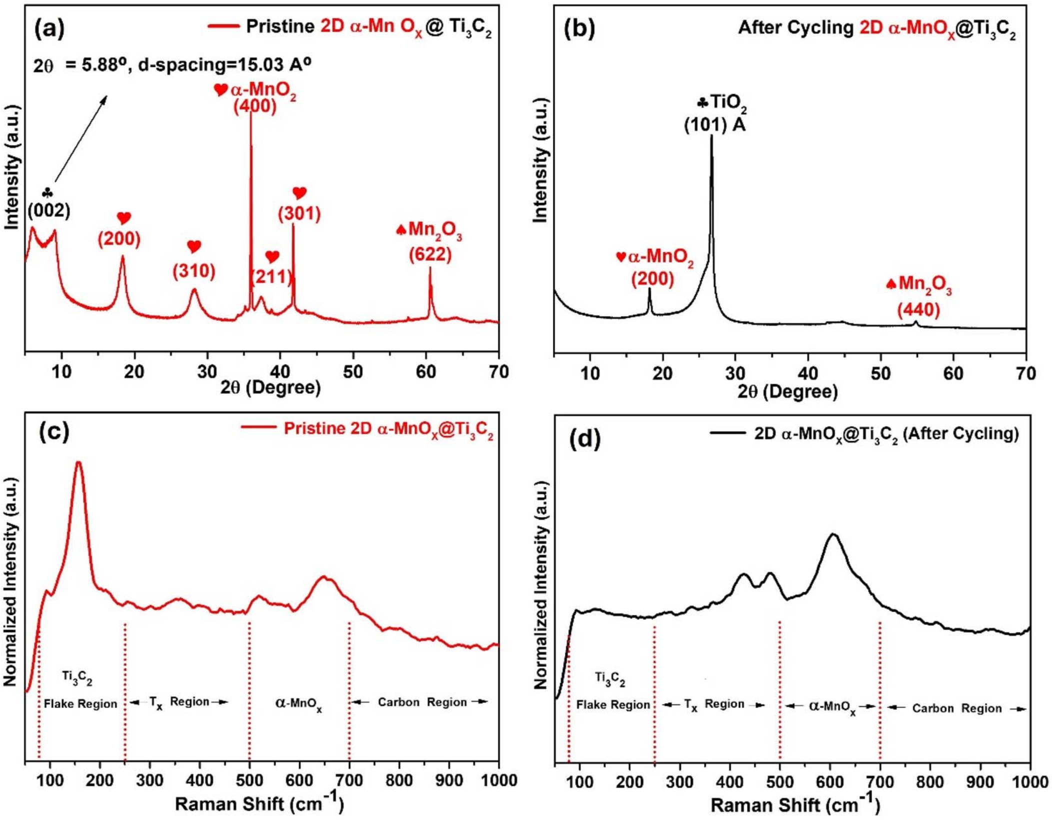

Fig. 1 (a) XRD spectra of pristine 2D α-MnO_x@Ti_3C_2 sample and after cycling in panel (b) Raman spectra of α-MnO_x@Ti_3C_2 sample before and after electrochemical cycling (c and d). The multilayer Raman peaks are deconvoluted before and after cycling.

multilayer Ti_3C_2, along with Mn–O vibrational modes linked to the nanosheet-like α-MnO_x domains.

After first discharge, several Raman modes become noticeably sharper and more distinct in both the M–Ti_3C_2 termination region (200–450 cm^{-1}) and the Mn–O stretching region (510–650 cm^{-1}), indicating a reorganization of surface functional groups on M–Ti_3C_2 and structural changes within the confined 2D α-MnO_2 layers. Deconvolution of the Raman spectra (Fig. 1c and d) shows the appearance of distinct vibrational bands of 2D α-MnO_x after cycling, suggesting enhanced ordering of the MnO_6 octahedra and a more stabilized MXene/2D α-MnO_x interfaces. An extra peak near 500 cm^{-1} after cycling is attributed to the A_{1g} mode (Ti–O) of TiO_2, indicating additional Ti oxidation. The 2D α-MnO_x bands around 600–650 cm^{-1} shift slightly lower and become broader with cycling, implying lattice distortions, defects, and strain relaxation.[19] These Raman signatures collectively reveal that cycling causes reorganization of termination groups, Ti oxidation, flake thinning, and 2D α-MnO_x structural disorder.[13,20]

A typical SEM image of the LiF-based molten-salt-etched MXene (Fig. 2a) reveals gaps between the Ti_3C_2 layers, confirming the successful removal of the aluminum layers. The etched Ti_3C_2 MXene forms an accordion-like multilayered structure after aluminum removal, exposing many surface functional groups (–F and –O) and yielding negatively charged M–Ti_3C_2 nanosheets. Additionally, 2D α-MnO_x nanosheets are grown *in situ* within the interlayers of M–Ti_3C_2 through a straight forward low-temperature DMSO-based process, as shown in Fig. 2b.

Highly conductive M–Ti_3C_2 MXene improves the conductivity of 2D α-MnO_x nanosheets, accelerating ion and electron transfer at the cathode. Fig. 2c and d show SEM images that confirm structural recovery, supporting the known mechanism of Li_2O_2 formation and decomposition in Ti_3C_2@MnO_x cathodes. The uniformly grown 2D α-MnO_x nanosheets are loosely aggregated, providing numerous active sites for Li-ion insertion and extraction (see Fig S2 more details). This demonstrates reversible morphological changes during discharge and charging in Li_2O_2 systems.

After discharging, the morphology, as shown in Fig. 2c and d, revealed dense toroidal and particle-like deposits, similar to Li_2O_2 toroids, surface films, and pore-blocking agglomerates reported on MnO_2-based electrodes.[11,21] Moreover, the multilayered Ti_3C_2 stacks display a typical accordion-like structure, consistent with previously observed discharge and charge behaviors of Ti_3C_2 MXene/MnO_2 composite cathodes in Li–O_2 batteries.[22,23] The α-MnO_x catalyzes Li_2O_2 nucleation, while the conductive Ti_3C_2 scaffold facilitates lateral growth, leading to thick deposits during discharge. Morphological and elemental changes after discharge show toroidal Li_2O_2 particles and Li_2O_2–MnO_x aggregates on the layered α-MnO_x@Ti_3C_2 surfaces, indicating oxygen reduction reaction (ORR) product formation (see Fig. S3 and S2 for additional details).

Fig. 3a shows the Mn 2p spectrum of the pristine sample, which can be decomposed into three oxidation states:

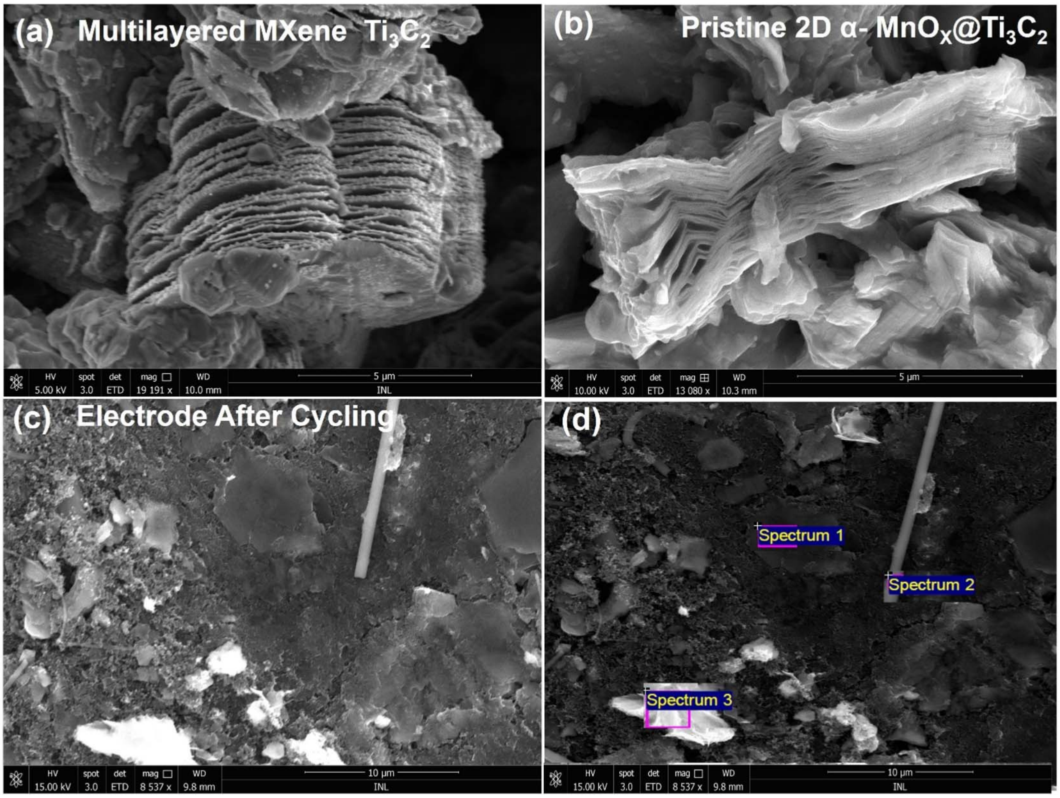

Fig. 2 SEM images showing: (a) etched Ti_3C_2 MXene, (b) fresh 2D α-MnO_x@Ti_3C_2, (c and d) display the electrode's morphology after cyclying.

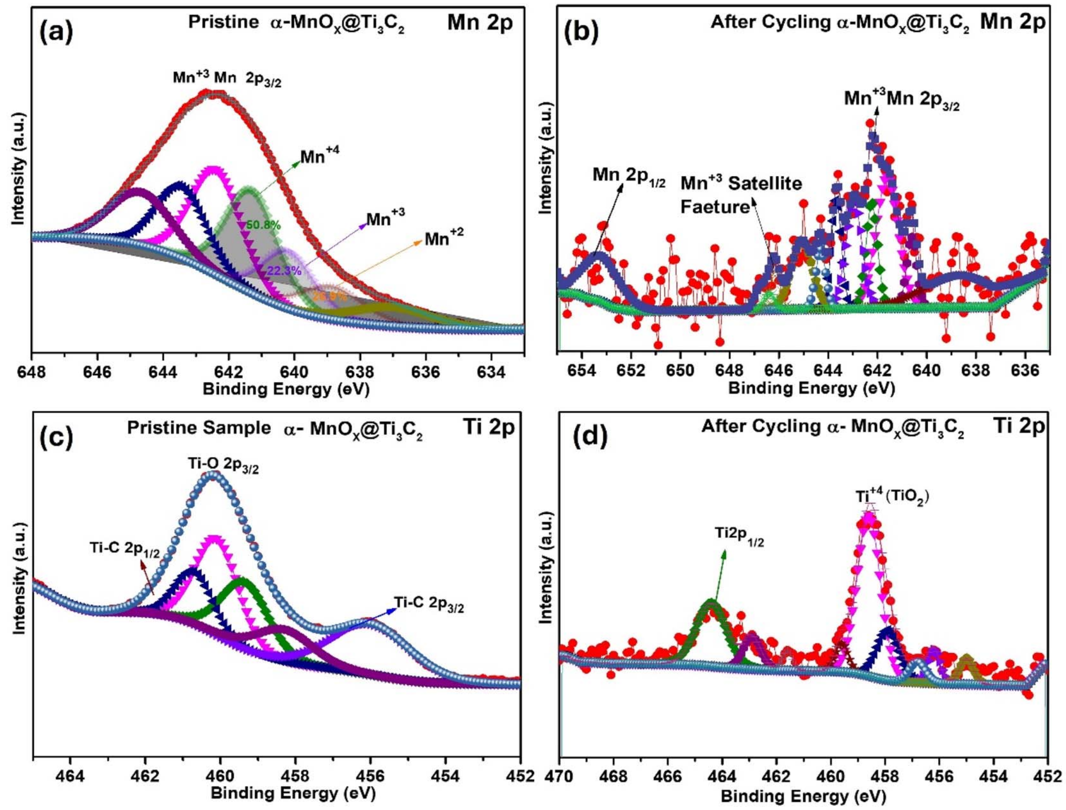

Fig. 3 High-resolution XPS spectra of Ti 2p and Mn 2p regions for the 2D α-MnO$_x$@M-Ti$_3$C$_2$before (a and c) and after (b and d) Li–O$_2$ cycling.

approximately 50.8% Mn^{4+} (2p$_{3/2}$ and 2p$_{1/2}$), 22.3% Mn^{3+}, and 26.9% Mn^{2+} based on peak areas. The predominant Mn^{4+} component (around ∼642–643 eV) suggests the material is mainly MnO$_2$-like, while the notable Mn^{3+} and Mn^{2+} signals (near ∼641 eV and ∼640–638 eV) indicate the nanosheets are partially reduced, forming a mixed-valence MnO$_x$ phase rather than a pure Mn^{4+} oxide. This variety in oxidation states is typical for solution-grown MnO$_x$ nanosheets. Consequently, a disordered α-MnO$_2$ chemically mixed valence MnO$_x$ nanosheet is also supported by our XRD data. The notable increase in Mn^{3+} peaks, along with their satellite features and a broad Mn^{2+} shoulder at lower binding energies, indicates that Mn^{4+} in α-MnO$_x$ was reduced to Mn^{3+} and Mn^{2+} during cycling. This reduction typically results from oxygen vacancies, Jahn–Teller distortion of Mn^{3+}, electrolyte-induced Mn dissolution, and collapse of the [2 × 2] tunnels that support the α-MnO$_2$ structure.[24] As these tunnels degrade and Mn shifts to lower oxidation states, the structure weakens, electronic conductivity decreases, and electrochemical reversibility diminishes. The diminished Mn^{4+} signal and the dominance of Mn^{3+}/Mn^{2+} in the XPS confirm that the electrode has transformed into a mixed-valence MnO$_x$ phase.

Additionally, the C 1s and O 1s spectra of both new and cycled samples were analyzed, with details in Fig. S2a–d. In the fresh α-MnO$_x$@Ti$_3$C$_2$ sample, the Ti 2p XPS spectrum mainly shows strong Ti–C peaks at ∼454.5 eV and ∼460.5 eV, along with only a small Ti–O peak near ∼458.5 eV. This indicates that the Ti$_3$C$_2$ MXene remains intact primarily with minimal surface oxidation. However, after Li–O$_2$ cycling, the Ti–O peak increases significantly while the Ti–C peaks decrease. This change suggests that part of the Ti$_3$C$_2$ surface is oxidizing to TiO$_2$ during operation, which may be the reason for the MXene structure to become chemically unstable during cycling and transformation into the poorly conductive TiO$_2$. This oxidation is primarily caused by reactive oxygen species produced during MnO$_x$ redox reactions and electrolyte decomposition, which lead to the breakdown of the Ti–C framework and the collapse of the multilayer structure. As a result, the loss of conductivity and structural integrity of Ti$_3$C$_2$ destabilized the embedded α-MnO$_x$ nanosheets, leading to rapid capacity decline and ultimately cell failure after 54 cycles.[25]

Galvanostatic charge/discharge curves were recorded for LAB cells using 2D α-MnO$_x$@M–Ti$_3$C$_2$ as air cathode at different current densities to assess the initial specific capacities and cycling stability as shown in Fig. 4. The initial specific discharge capacities of 2D α-MnO$_x$@M–Ti$_3$C$_2$ of 14 377, 12 648, and 11 242 mA g^{-1} at varying current densities of 100, 200, and 300 mA g^{-1}, respectively presented in Fig. 4a. The performance of the electrode is remarkable compared with MnO$_2$-based electrocatalysts under similar testing conditions. At 100 mA g^{-1}, the produced capacity is higher than that of a similar system reported in the literature (Table S1). The overall electrochemical reaction occurring during the charge and discharge of the LAB is presented in eqn (1). During discharge, Li$_2$O$_2$ is formed as a result of the oxygen reduction reaction (ORR), whereas during

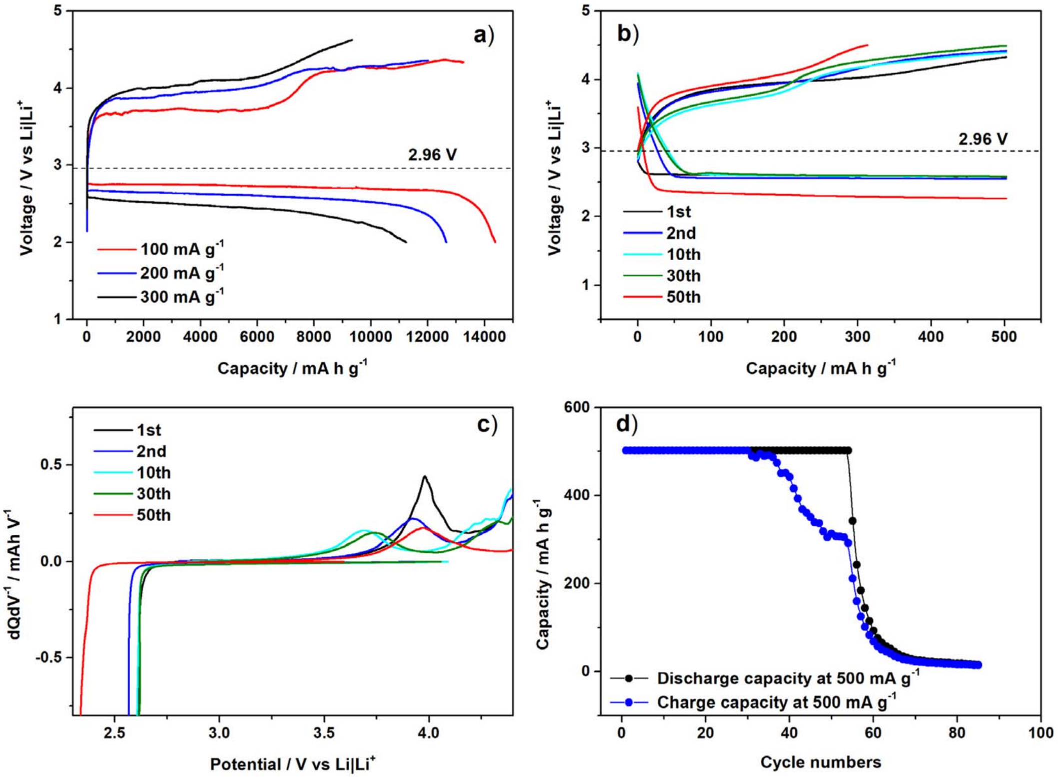

Fig. 4 Electrochemical performances of LABs with 2D α-MnO_x@M-Ti_3C_2. (a) Discharge/charge profiles at 100, 200 and 300 mA g^{-1}, and (b) at different cycles at 500 mA g^{-1} with fixed specific capacity of 500 mAh g^{-1}. (c) d*Q*/d*V* profile of discharge/charge curves at different cycles. (d) Complete cyclability obtained at 500 mA g^{-1} and 500 mAh g^{-1}.

charging, lithium peroxide is decomposed through the oxygen evolution reaction (OER).[26]

$$2Li + O_2 + 2e^- \rightleftharpoons Li_2O_2 \; E = 2.96 \text{ V } vs. \text{ Li}^+/\text{Li} \quad (1)$$

The onset potentials for the discharge (ORR) were found to be at 2.75, 2.68 and 2.59 V *vs.* Li^+/Li, at 100, 200, and 500 mA g^{-1}, respectively. While for the charge (OER) the values were 3.66, 3.85 and 3.92 V *vs.* Li+/Li, at 100, 200, and 500 mA g^{-1}, respectively, indicating the outstanding catalytic activity promoted by the synergic effect between the M–Ti_3C_2 MXene and 2D α-MnO_x nanosheets (see Table S2). The coexistence of Mn^{3+} and Mn^{4+} generates a flexible electronic environment that enhances both charge compensation and electron transfer during electrochemical cycling. During ORR (discharge), Mn^{4+} is reduced to Mn^{3+}, accepting electrons and facilitating O_2 activation into superoxide-like intermediates, whereas during OER (charge), Mn^{3+} is oxidized back to Mn^{4+}, enabling efficient electron extraction from Li_2O_2 and lowering the associated overpotential relative to fixed-valence oxides. In parallel, the mixed-valence configuration promotes electronic conductivity through a double-exchange mechanism (Mn^{3+}–O–Mn^{4+}), which enables electron hopping between adjacent cations and improves charge transfer to and from surface-bound intermediates.[27,28] At the atomic level, Mn^{3+} in an octahedral crystal field exhibits a high-spin d^4 (t_{2g}^3 e_g^1) configuration, where the singly occupied e_g orbital is aligned along the metal–oxygen bond axis, directly influencing adsorption behavior. This electronic structure weakens LiO_2 adsorption by increasing electron density in O_2 antibonding orbitals, resulting in moderate binding that is favorable for OER by preventing surface poisoning, while excessively strong adsorption, as in Mn^{4+}-dominated sites, would hinder reaction kinetics.[29,30]

Additionally, the e_g^1 configuration of Mn^{3+} induces Jahn–Teller distortion, producing a locally flexible coordination environment that accommodates structural changes during Li_2O_2 formation. This flexibility reduces lattice mismatch during nucleation, promoting the growth of less crystalline and more defective Li_2O_2 morphologies that are easier to decompose upon charging, in contrast to the dense films typically associated with Mn^{4+}-rich systems. The overall catalytic performance is therefore governed by the synergistic interaction between Mn^{3+} and Mn^{4+} sites rather than by either species alone. During ORR, O_2 adsorption and activation occur at Mn^{3+}–Mn^{4+} pairs, where Mn^{4+} polarizes the molecule and Mn^{3+} facilitates electron donation to form O_2^-, enabling subsequent Li^+ coordination without over-stabilizing intermediates.[31,32] Conversely, during OER, Li_2O_2 decomposition proceeds *via* LiO_2 intermediates that are optimally stabilized at Mn^{3+} sites strong enough to sustain transient species yet weak enough to allow their further transformation and O_2 evolution. This balance between stabilization and reactivity, achieved through mixed valence, underpins the improved catalytic efficiency compared to single-valence manganese oxides.[33,34]

Furthermore, high current densities help suppress parasitic reactions but lead to higher overpotentials. This behavior may be linked to the reaction interface, where Li_2O_2 tends to detach from the electrode surface under high current conditions.[23,35] It is important to emphasize that the reaction interface during charging is highly dependent on both the charge rate and the applied voltage; specifically, high rates and overpotentials promote O_2 evolution at the Li_2O_2, *i.e.*, electrode interface, which in turn contributes to detachment of the remaining Li_2O_2 from the electrode.[21,22]

The cyclability of the LAB cells is investigated using a capacity-limited strategy that restricts the discharge capacity to 500 mAh g^{-1} at 500 mA g^{-1}. Fig. 4b illustrates the evolution of the battery's discharge/charge profile over cycling, while coulombic efficiency is presented in Fig. S5. During the initial cycles (up to ~30 cycles), both discharge and charge capacities remain close to the defined limit, indicating good reversibility and efficient formation and decomposition of Li_2O_2 *via* the ORR and OER, respectively. However, beyond this region, the charge capacity begins to decline gradually, while the discharge capacity remains relatively stable before eventually decreasing. This divergence suggests increasing polarization and reduced charge efficiency, likely due to the incomplete decomposition of Li_2O_2 and the accumulation of parasitic side products such as Li_2CO_3. As cycling progresses (50–65 cycles), both charge and discharge capacities exhibit a sharp decline, signaling severe electrode degradation. This rapid capacity fading can be attributed to the buildup of insulating discharge products, pore blockage, and hindered oxygen diffusion, which collectively limit active reaction sites and electron transport. The high applied current density further exacerbates these effects by promoting non-uniform, film-like Li_2O_2 deposition and accelerating electrolyte decomposition. Ultimately, the near-total loss of capacity after ~65 cycles indicates cell failure, highlighting the challenges associated with maintaining stable cycling performance in lithium–air batteries under high-rate conditions. The total overpotentials measured at 100 mAh g^{-1} reached during the 1st, 2nd, 10th, 30th, and 50th cycles are 1.244, 1.259, 1.015, 1.038, and 1567 V, respectively.

Fig. 4c presents the dQ/dV curves obtained from the charge/discharge profiles. The discharge onset voltage is initially 2.628 V, compared to the theoretical 2.96 V. This voltage shows a significant shift from 2.582 V to 3.620 V between the 2nd and 10th cycles. The cell exhibits a peak at 3.616 V up to the 30th charge, which shifts to 2.398 V by the 50th cycle, accompanied by a notable decrease in peak intensity. This behavior indicates a rapid loss of voltage control and an immediate decline in cell performance.

Finally, as shown in Fig. 4d, the 2D α-MnO_x@M–Ti_3C_2 sample can undergo 54 consecutive cycles, representing an improvement over similar MXene[36] and MnO_2 structures (Table S1). Up to approximately the 30th cycle, the difference between the charge and discharge voltages remained relatively small, in which the electrode structural stability seems to have a considerable influence in the discharge/charge cycle reversibility. However, as the 54th discharge cycle approached, the discharge voltage dropped sharply to 1.5 V, at which point the charging process was terminated. It can be correlate to the XPS result that after cycling, the Mn 2p XPS spectrum indicates that the original α-MnO_x undergoes significant reduction and structural breakdown, which explains the rapid capacity decline after 54 cycles.

In conclusion, a simple, one-step, oxidant-free method has been developed to engineer mixed-valence MnO_x directly within MXene layers during delamination. Our SEM results show that 2D α-MnO_x nanosheets successfully grew within the etched interlayer spaces of multilayer Ti_3C_2 MXene during low-temperature delamination under constant magnetic stirring. Electrochemical results indicate that the high electrical conductivity of the 2D α-MnO_x@Ti_3C_2 catalyst allows for rapid electron transport during LAB operation, achieving a high specific capacity and maintaining stable cycling over 54 cycles at a higher current density. It is believed that the interlaced 2D hybrid nanosheet structure exposes more active sites and provides additional space for Li_2O_2 deposition. As a result, the ORR/OER reaction kinetics in the LAB are improved, enhancing overall electrochemical performance. This strategy offers a versatile platform for confined redox chemistry of metal oxides within MXenes and enables high-performance energy storage electrodes for Li–O_2 batteries.

Author contributions

Aqrab ul Ahmad: concept, investigation, experimental materials synthesis, writing original draft. William G. Morais: investigation, battery analysis, writing original draft. Tauqeer Ahmad: formal analysis, origin graphs. Ihsan Çaha: microscopy, review & editing. Isilda Amorim: crystallographic analysis, Siva Sankar Nemala: spectroscopic data analysis and editing, resources, Francis Leonard, Deepak: supervision, funding acquisition, project administration, review & editing.

Conflicts of interest

The authors declare no competing financial interests.

Data availability

The data supporting this article have been included as part of the supplementary information (SI). Supplementary information: experimental section and more details on characterization related to SEM, XPS and Raman spectroscopy analysis carried out on the samples. See DOI: https://doi.org/10.1039/d6ta01055e.

Acknowledgements

We acknowledge financial support from the European Union (Grant FUNLAYERS – 101079184). This article is a result of the Innovation Pact "NGS – New Generation Storage" (C644936001-00000045), by "NGS" Consortium, co-financed by Next Generation EU from the European Union, through the Incentive

System "Agendas for Business Innovation" ("Agendas para a Inovação Empresarial"), within the Recovery and Resilience Plan (PRR).

References

1 Y. Ding, Y. Li, M. Wu, H. Zhao, Q. Li and Z. Wu, *Energy Storage Mater.*, 2020, **31**, 470–491.

2 S. Karunarathne, C. K. Malaarachchi, A. M. Abdelkader and A. R. Kamali, *J. Power Sources*, 2024, **607**, 234553.

3 J. W. Jung, S. H. Cho, J. S. Nam and I. D. Kim, *Energy Storage Mater.*, 2020, **24**, 512–528.

4 T. Liu, J. P. Vivek, E. W. Zhao, J. Lei, N. Garcia-Araez and C. P. Grey, *Chem. Rev.*, 2020, **120**, 6558–6625.

5 J. Lai, Y. Xing, N. Chen, L. Li, F. Wu and R. Chen, *Angew. Chem., Int. Ed.*, 2020, **59**, 2974–2997.

6 J. Zhao, R. Pathak, Z. Zhao, X. Chen, M. B. Saud, H. Li, F. Wu, Q. Qiao, J. W. Elam and X. Wang, *Green Chem.*, 2023, **25**, 10182–10208.

7 B. Liu, Y. Sun, L. Liu, S. Xu and X. Yan, *Adv. Funct. Mater.*, 2018, **28**, 1–34.

8 A. Perner, K. Holl, D. Ilic and M. Wohlfahrt-Mehrens, *Eur. J. Inorg. Chem.*, 2002, **2002**, 1108–1114.

9 J. Read, *J. Electrochem. Soc.*, 2002, **149**, A1190.

10 T. Ogasawara, A. Débart, M. Holzapfel, P. Novák and P. G. Bruce, *J. Am. Chem. Soc.*, 2006, **128**, 1390–1393.

11 K. Adpakpang, S. M. Oh, D. A. Agyeman, X. Jin, N. Jarulertwathana, I. Y. Kim, T. Sarakonsri, Y. M. Kang and S. J. Hwang, *Adv. Funct. Mater.*, 2018, **28**, 1–11.

12 Y. Lin, Y. Li, M. Tang, L. Zhan, Y. Zhai, W. Chen, M. Zhou, Y. Ji and P. Wang, *Inorganica Chim. Acta*, 2024, **572**, 122239.

13 Y. Li, D. Xu, D. Zhang, Y. Wei, R. Zhang and Y. Guo, *RSC Adv.*, 2019, **9**, 33572–33577.

14 Q. Xue, Z. Pei, Y. Huang, M. Zhu, Z. Tang, H. Li, Y. Huang, N. Li, H. Zhang and C. Zhi, *J. Mater. Chem. A*, 2017, **5**, 20818–20823.

15 Q. Sun, Z. Guo, T. Shu, Y. Li, K. Li, Y. Zhang, L. Li, J. Ning and K. X. Yao, *ACS Appl. Mater. Interfaces*, 2024, **16**, 12781–12792.

16 X. Guo, S. Yang, D. Wang, A. Chen, Y. Wang, P. Li, G. Liang and C. Zhi, *Curr. Opin. Electrochem.*, 2021, **30**, 100769.

17 S. E. Pas, R. Banavath, M. Dujovic, M. Radovic, J. L. Lutkenhaus and M. J. Green, *Adv. Mater. Interfaces*, 2025, **12**, e00355.

18 A. Sarycheva and Y. Gogotsi, *Chem. Mater.*, 2020, **32**, 3480–3488.

19 C. Julien, M. Massot, S. Rangan, M. Lemal and D. Guyomard, *J. Raman Spectrosc.*, 2002, **33**, 223–228.

20 T. Gao, H. Fjellvåg and P. Norby, *Anal. Chim. Acta*, 2009, **648**, 235–239.

21 Y. Zheng, K. Song, J. Jung, C. Li, Y. U. Heo, M. S. Park, M. Cho, Y. M. Kang and K. Cho, *Chem. Mater.*, 2015, **27**, 3243–3249.

22 L. Wang, Y. Zhang, Z. Liu, L. Guo and Z. Peng, *Green Energy Environ.*, 2017, **2**, 186–203.

23 S. Wu, J. Tang, F. Li, X. Liu and H. Zhou, *Chem. Commun.*, 2015, **51**, 16860–16863.

24 J. Duan, M. Huang, M. Song, W. Zhou and H. Tan, *Materials*, 2025, **18**, 2817.

25 J. Tang, T. S. Mathis, N. Kurra, A. Sarycheva, X. Xiao, M. N. Hedhili, Q. Jiang, H. N. Alshareef, B. Xu, F. Pan and Y. Gogotsi, *Angew. Chem., Int. Ed.*, 2019, **58**, 17849–17855.

26 L. Liu, Y. Liu, C. Wang, X. Peng, W. Fang, Y. Hou, J. Wang, J. Ye and Y. Wu, *Small Methods*, 2022, **6**, 2101280.

27 Y. J. Lee, D. H. Kim, T.-G. Kang, Y. Ko, K. Kang and Y. J. Lee, *Chem. Mater.*, 2017, **29**, 10542–10550.

28 C. Chowde Gowda, A. Mathur, A. Parui, P. Kumbhakar, P. Pandey, S. Sharma, A. Chandra, A. K. Singh, A. Halder and C. S. Tiwary, *J. Ind. Eng. Chem.*, 2022, **113**, 153–160.

29 E. Pargoletti, A. Salvi, A. Giordana, G. Cerrato, M. Longhi, A. Minguzzi, G. Cappelletti and A. Vertova, *Nanomaterials*, 2020, **10**, 1735.

30 Z. Awan, Z. K. Ghouri and S. Hashmi, *Int. J. Hydrogen Energy*, 2018, **43**, 2930–2942.

31 C. M. Julien and A. Mauger, *Nanomaterials*, 2017, **7**, 396.

32 T. Subramaniam, B. S. Krishnaveni and S. Devaraj, *J. Mater. Sci. Mater. Electron.*, 2024, **35**, 1184.

33 M. Rabe, C. Toparli, Y.-H. Chen, O. Kasian, K. J. J. Mayrhofer and A. Erbe, *Phys. Chem. Chem. Phys.*, 2019, **21**, 10457–10469.

34 S. E. Balaghi, C. A. Triana and G. R. Patzke, *ACS Catal.*, 2020, **10**, 2074–2087.

35 M. Chao, K. Zeng, C. Lu, Z. Shi, J. Guo, X. Chen and R. Yang, *J. Colloid Interface Sci.*, 2024, **657**, 46–53.

36 C. Wen, T. Zhu, X. Li, H. Li, X. Huang and G. Sun, *Chinese Chem. Lett.*, 2020, **31**, 1000–1003.